Investigation of flow control and cooling performance using comb plasma actuators

Jie Sun
Hebei University of Technology
Jin Wang (wjwcn00@163.com)
Hebei University of Technology
Gongnan Xie
Northwestern Polytechnical University
Bengt Sundén
Lund University

Research Article

Keywords: aerodynamic actuation, comb electrode, film cooling, flow control, plasma, pressure loss

Posted Date: January 23rd, 2023

DOI: https://doi.org/10.21203/rs.3.rs-2497702/v1

Additional Declarations: No competing interests reported.

Investigation of flow control and cooling performance using comb plasma actuators

Jie Sun, Jin Wang*, Gongnan Xie*, Bengt Sundén

Jie Sun

School of Energy and Environmental Engineering, Hebei University of Technology, Tianjin 300401, China

E-mail: jiesun@mail.nwpu.edu.cn

Jin Wang

1. School of Energy and Environmental Engineering, Hebei University of Technology, Tianjin 300401, China

2. Key Laboratory of Thermo-Fluid Science and Engineering (Xi'an Jiaotong University), Ministry of Education, Xi'an 710049, China

*Corresponding author: wjwcn00@163.com

Gongnan Xie

School of Marine Science and Technology, Northwestern Polytechnical University, Xi'an 710072, China

*Corresponding author: xgn@nwpu.edu.cn

Bengt Sundén

Department of Energy Sciences, Division of Heat Transfer, Lund University, Lund SE-22100, Sweden

E-mail: bengt.sunden@energy.lth.se

Abstract

This paper proposes a novel comb plasma actuator (CPA) for active flow control. The effects of the CPA on the tip and the root are investigated to improve the film cooling effectiveness. Results show that the CPA on the root increases the size of the counter-rotating vortex pairs (CRVPs) and the agminated body force arches the coolant air away from the wall. Nevertheless, the scale of the anti-counter rotating vortex pairs (Anti-CRVPs) induced by CPA on the tip is larger than one of CRVPs, which significantly weakens the coiling effect of the mainstream on the coolant air. The maximum velocity of the near-wall fluid with CPA on the tip is 1.2 times that without a plasma actuator. Compared with plasma off, the wall-averaged film cooling effectiveness increases by 90.9%, 108.9%, 87.2%, and 38.0%, respectively, under blowing ratios of 0.25, 0.5, 0.75, and 1.0 when using CPA on the tip. In addition, the wall-averaged cooling effectiveness increases by 58.7%, 108.9%, and 115.0% when applied voltages are 6 kV, 12 kV, and 24 kV%, respectively. The diffusing body force of CPA on the tip increases coolant air distributions along the spanwise direction. When the blowing ratio increases from 0.25 to 1.0, the spanwise film cooling effectiveness increases by 62.3%, 103.4%, 164.6%, and 150.5%, respectively, on average.

Keywords: aerodynamic actuation, comb electrode, film cooling, flow control, plasma, pressure loss

NOMENCLATURE

A	Amplitude of exposed electrode, mm
a	Normal height of the plasma region, mm
b	Streamwise length of the plasma region, mm
D	Diameter of film cooling hole, mm
DR	Coolant air to mainstream density ratio， ρ_c/ρ_∞
E	Electric field intensity, kV/cm
E_b	Breakdown electric field intensity, kV/cm
e_c	Elementary charge, C
F	Body force, mN/mm^3
f	Frequency of applied voltage, kHz
k_1, k_2	Spatial distribution coefficient of the electric field
L_1	Width of exposed electrode, mm
L_2	Width of covered electrode, mm
L_3	Spanwise length of the electrode, mm
M	Blowing ratio, $DR \cdot U_c/U_\infty$
s	Spacing between the electrodes, mm
T	Local fluid temperature, K
U	Streamwise velocity of jet flow, m/s
W	Normal velocity of jet flow, m/s
X, Y, Z	Coordinate direction distance, mm
Greek symbols	
Δ	Growth rate of film cooling effectiveness
Δt	Charge time of plasma, μs
η	Film cooling effectiveness
Θ	Dimensionless temperature
λ	Wavelength of exposed electrode, mm
ρ_c	Charge density, C/m^3
φ	Applied voltage, kV
Subscripts	
aw	Adiabatic wall
c	Coolant air
s	Value along the spanwise direction
w	Value along the wall
∞	Mainstream
Abbreviations	
Anti-CRVPs	Anti-counter rotating vortex pairs
CPA	Comb plasma actuator
DBD	Dielectric barrier discharge

1. Introduction

Air pollution caused by conventional thermal power generation is a prominent problem [1]. The proposals for carbon neutrality and peak carbon dioxide emissions have led to a booming opportunity for gas turbines [2]. The cooling air required to cool the hot end components of the gas turbine derives from the compressor. Increasing the utilization of cooling air is conducive to reducing fuel consumption, which has positive implications for alleviating the current energy crisis and environmental degradation [3]. While advanced film cooling technology holds tremendous advantages in reducing the amount of cooling air, it limits cooling capacity [4].

Some researchers have focused on the effect of plasma actuation on flow control. Compared with passive flow control, such as vortex generators [5] and transverse trenches [6], active flow control using plasma actuators shows favorable characteristics, such as quick response [7], small size [8], and low power consumption [9]. Li et al. [10] indicated that the dielectric barrier discharge (DBD) plasma actuation accelerated the near-wall fluid flow. Zhang et al. [11] analyzed the start-up stage of the flow field under plasma actuation using schlieren visualization and particle image velocimetry. It was found that the plasma actuator produced a thin jet in the first stage, and an arched jet escaped from the surface in the second stage. The starting vortex controlled the induced flow field, and the arched jet disappeared in the third stage. In the fourth stage, the wall-jet played a dominant role in the induced flow field, and the deflection angle of the wall-jet was approximately constant. Chen et al. [12] analyzed the flow control effect of annular plasma actuator. Results revealed that the flow state changes from laminar to turbulent in advance due to the rotating vortex ring generated by the annular plasma actuator in the opposite direction to the external air recirculation. Harinaldi et al. [13] experimentally studied the effect of plasma on flow control using a delta wing with a 65° sweep angle. It was found that the lift coefficient of the delta wing increased by 0.078, and the drag coefficient decreased by 0.053 under multiple plasma actuators. Huang et al. [14] investigated the effect of plasma actuators on flow control under a laminar separation condition. Results showed that compared with plasma off, the flow energy during one oscillation period was reduced by 726% with a co-current plasma actuator at the position of 0.6 chord from the leading edge. Plasma actuation effectively alleviated the pitch instability of laminar separation flutter at a high Reynolds number of 77,000. Zheng et al. [15] analyzed two flow control principles of alternating current (AC) plasma and nanosecond plasma both numerically and experimentally. Results indicated that the wall jet at the AC plasma discharge only affected the fluid flow near the actuator. In contrast, the flow field downstream the actuator was affected by the waste heat generated by the nanosecond plasma discharge. Giorgi et al. [16] analyzed the effect of plasma actuation on flow separation of compressor cascades. Results showed that the plasma aerodynamic actuation caused 14% reduction of the pressure loss coefficient and 3% increase in the static pressure.

The plasma actuator was arranged on the gas turbine blade based on active flow control to enhance the film cooling performance [17]. Dai et al. [18] studied effect of plasma aerodynamic actuation on a circular jet in cross flow field by using Smoke Visualization technology. Results showed that trend of the circular jet to stick to the wall became obvious with increasing applied voltage. The large arc length of the exposed electrode at the hole outlet increased the effusion effect of the jet near the wall. Erfani et al. [19] analyzed the effect of plasma actuator temperature on thermodynamic performance. Results revealed that the maximum induced velocity of the hot medium actuator increased by 45.5% compared to that of the cold medium actuator. The shape of the plasma actuator has immensely affected aerodynamic actuation effect. Li et al. [20] investigated the effect of a sawtooth plasma actuator (STPA) on the film cooling using a plasma phenomenological model. Results showed that the film cooling effectiveness of the STPA on the tip was 65.5% higher than that of STPA on the root. Durscher and Roy [21] analyzed the disturbance of the flow field by circular and rectangular plasma actuators using particle image velocimetry. Results showed that the flow field induced by the two plasma actuators presented a spiral structure.

Although many scholars have focused on effect of plasma on active flow control and film cooling, few of them were related to convective heat transfer enhancement by using different shapes of plasma actuators. In this work, propose a new comb plasma actuator (CPA) is proposed and the thermodynamic performance is investigate. Based on the plasma model proposed in Shyy et al. [22], the electric body force as a source term is coupled to the momentum equation to achieve the plasma aerodynamic actuation. This research investigates the effects of the CPA on the tip and the CPA on the root on flow field disturbances and heat transfer enhancement by analyzing vortex structures near the film hole. These results create a foundation for improving film cooling performance based on the plasma actuation for the active flow control.

2. Model introduction and validation

This section introduces the computational domain, plasma model, boundary conditions, and governing equations.

2.1 Geometry and plasma actuator

Fig. 1 shows the three-dimensional computational domain in this research. A film hole with a diameter (*D*) of 12.7 mm has a length of 4*D* and an inclination angle of 35º. The size of the mainstream channel is 59*D*×3*D*×10*D*, and the trailing edge of the film hole outlet is 40*D* away from the mainstream outlet. The coolant chamber has a length of 6*D*, a width of 3*D*, and a height of 6*D*. The origin of coordinates is located at the trailing edge of the film hole outlet. The axes *X*, *Y*, and *Z* represent the streamwise direction, spanwise direction and normal direction of the airflow.

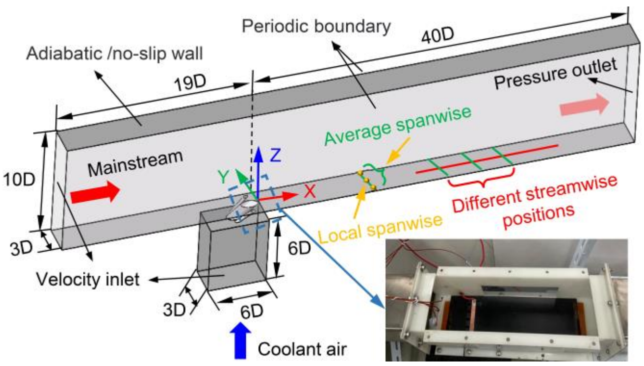

Fig. 1 Three-dimensional computational domain

Fig. 2 shows a schematic diagram of comb plasma actuators on tip and root in the numerical simulation. The exposed and covered electrodes are arranged asymmetrically on both sides of the flat plate. The bottom of the covered electrode is covered with an insulating layer to prevent plasma discharge. Table 1 presents the parameters of the comb plasma actuator. The exposed electrode has a length (L_1) of 12 mm, amplitude (*A*) of 8 mm, and wavelength (λ) of 12.7 mm. The length (L_2) of the covered electrode is

20 mm, and the width (L_3) is 38.1 mm. The distance (s) between the exposed and covered electrodes is 1 mm, and the thickness is 0.1mm. The plasma region has dimensions of 3 mm in height and 6 mm in length.

Body force distributions induced by CPA are shown in Fig. 2. The CPA on the tip has the expended body force along the spanwise direction, whereas the CPA on the root has an agminated body force toward the wall center. According to the plasma phenomenological model by Shyy et al. [22], the body force from the actuator is added to the momentum equation through user-defined functions (UDFs) in ANSYS Fluent software as a source term. The plasma region is located in the triangular prism region of the flat plate, and its active flow control is reflected by the acceleration of near-wall fluid ejection.

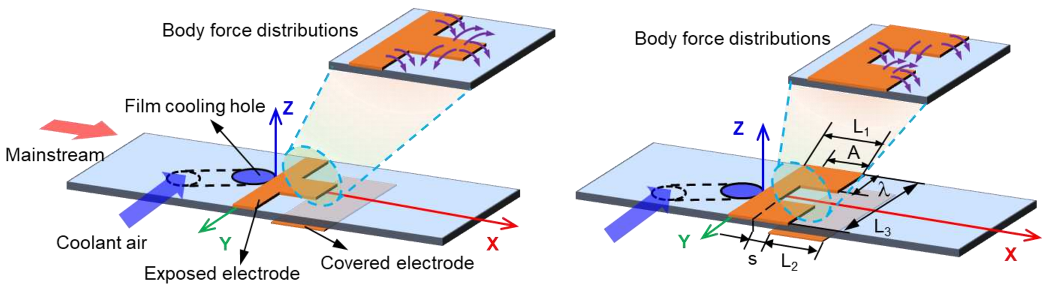

(a) CPA on tip (b) CPA on root

Fig. 2 Arrangeme nts and body force distributions of comb plasma actuators

Table 1. Parameters of comb plasma actuators

Parameters	Values
Normal height of the plasma region (a)	3 mm
Amplitude of exposed electrode (A)	8 mm
Streamwise length of the plasma region (b)	6 mm
Applied frequency of plasma actuator (f)	2 kHz
Width of the exposed electrode (L_1)	5 mm
Width of the covered electrode (L_2)	10 mm
Spanwise length of the electrode (L_3)	38.1 mm
Spacing between the electrodes (s)	0.5 mm
Wavelength of the exposed electrode (λ)	12.7 mm
Thickness of two electrodes	0.1 mm

2.2 Boundary conditions

Table 2 presents the boundary conditions of the simulations. The mainstream and the coolant air are assumed to be incompressible ideal gases, and the inlets of the mainstream channel and coolant chamber are set as velocity inlet boundaries. The inlet temperature values of the mainstream (T_∞) and the coolant air (T_c) are given at 300 K and 200 K, respectively, and the inlet velocity of the mainstream (U_∞) is 20 m/s. The density ratio (DR) of the mainstream to the coolant air is 1.5. The channel outlet is set as a pressure outlet boundary with a pressure value of 101,325 Pa. Periodic boundary conditions are applied for both sides of the mainstream channel and the coolant chamber. Adiabatic no-slip boundary condition is set on other walls.

Table 2. Boundary conditions of simulations

Parameters	Values
Temperature of mainstream inlet (T_∞)	300 K
Inlet velocity of mainstream (U_∞)	20 m/s
Outlet pressure (P)	101,325 Pa
Temperature of coolant air inlet (T_c)	200 K
Density ratio (DR)	1.5
Blowing ration (M)	0.25, 0.5, 0.75, 1.0

2.3 Governing equations

Fig. 3 presents a schematic diagram of the plasma aerodynamic actuation. The plasma power supply generates an alternating current at high frequency and high pressure. The air molecules are ionized above the covered electrode. Outer electrons escape from the nucleus and become free electrons. The plasma consists of positive nuclei and negative free electrons. The plasma collides with surrounding air molecules to exchange momentum under the electric field, and the air above the electrode is constantly ionized [23]. The fluid shows a trend to rush towards the wall under the aerodynamic actuation of the plasma actuators. The electric field intensity in the phenomenological model is linearized by Shyy et al. [22]. The plasma is full of the triangular region AOB in Fig. 3.

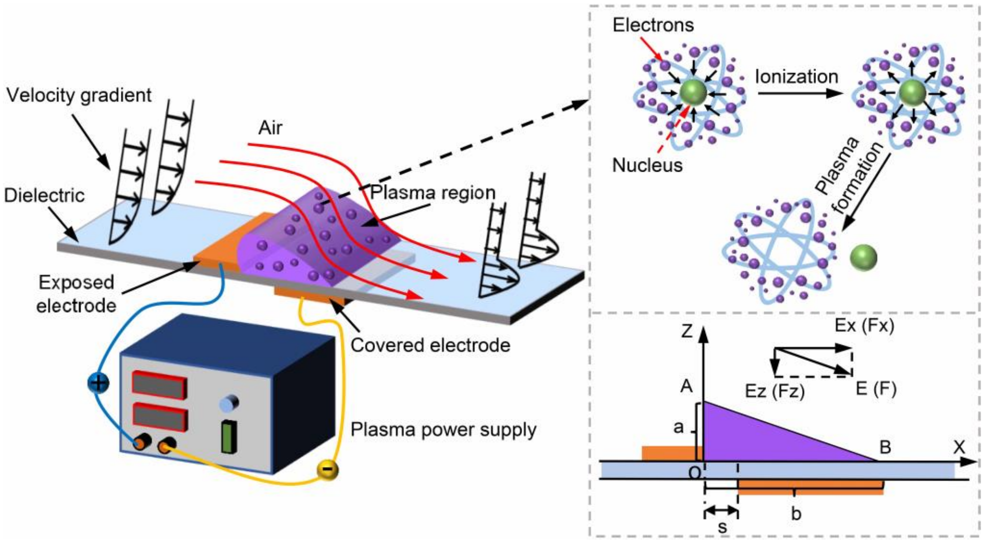

Fig. 3 Schematic diagram of the plasma aerodynamic actuation

According to Ref. [22], the electric field intensity decreases linearly along the coordinate axis, and it is calculated by:

$$E(X,Z)=\left|\vec{E}\right|=E_0-k_1X-k_2Z \tag{1}$$

$$k_1=\frac{E_0-E_b}{b} \tag{2}$$

$$k_2=\frac{E_0-E_b}{a} \tag{3}$$

where E_0 represents the ratio of applied voltage (φ_0) to electrode gap (s). k_1 and k_2 are spatial distribution coefficients of the electric field intensity, which refers to the spatial distribution gradient of the electric field intensity. In the present simulation, the breakdown electric field intensity E_b is 30 kV/cm. The components of the electric field in the directions X and Z are defined as:

$$E_x(X,Z)=\frac{E(X,Z)k_2}{\sqrt{k_1^2+k_2^2}} \tag{4}$$

$$E_z(X,Z) = \frac{E(X,Z)k_1}{\sqrt{k_1^2 + k_2^2}} \tag{5}$$

where the body force components in the directions *X* and *Z* are given by:

$$F_X = \rho_c e_c f \Delta t E_X \tag{6}$$

$$F_Z = \rho_c e_c f \Delta t E_Z \tag{7}$$

there the charge density ρ_c is 10^{17} C/m^3, and elementary charge e_c is 1.6×10^{-19} C. The applied frequency (*f*) is 2 kHz, and duration of plasma actuation (Δt) is 67 μs. Other detailed parameters can be found in Ref. [22].

In the book by Versteeg and Malalasekera [24] the mass conservation equation, momentum equation, and energy equation are presented as follows:

$$\frac{\partial}{\partial x_i}(\rho u_i) = S_m \tag{8}$$

$$\frac{\partial}{\partial x_i}(\rho u_i u_j) = -\frac{\partial P}{\partial x_j} + \frac{\partial}{\partial x_i}(\tau_{ij} - \rho \overline{u_i' u_j'}) + \rho \vec{g} + F_j \tag{9}$$

$$\frac{\partial}{\partial x_i}(\rho c_p u_i T) = \frac{\partial}{\partial x_i}(\lambda \frac{\partial T}{\partial x_i} - \rho c_p \overline{u_i' T'}) + \mu \phi + S_h \tag{10}$$

where S_m, F_j, and S_h are source terms in the mass, momentum, and energy equations. F_j represents the electric field force induced by the plasma actuator. As a source term of the steady body force, F_j is added to the momentum equation through the user-defined functions (UDFs) in the software ANSYS Fluent 18.0. The electric field strength and the body force are stored in the user-defined memories (UDMs) for post-processing.

According to Goldstein et al. [25], the blowing ratio is defined by:

$$M = \frac{\rho_c U_c}{\rho_\infty U_\infty} = DR \frac{U_c}{U_\infty} \tag{11}$$

where DR is the density ratio of coolant air to the mainstream. ρ is density, and U is flow velocity. c represents coolant air, and ∞ represents mainstream. The film cooling effectiveness is calculated by:

$$\eta = \frac{T_{\infty} - T_{aw}}{T_{\infty} - T_{c}} \tag{12}$$

where T_{∞} and T_c represent the inlet temperature of mainstream and coolant air, respectively. T_{aw} means adiabatic wall temperature. Spanwise-averaged film cooling effectiveness ($\overline{\eta_s}$) and wall-averaged film cooling effectiveness ($\overline{\eta_w}$) are given by:

$$\overline{\eta_s} = \frac{T_{\infty} - \overline{T_{s-aw}}}{T_{\infty} - T_{c}} \tag{13}$$

$$\overline{\eta_w} = \frac{T_{\infty} - \overline{T_{w-aw}}}{T_{\infty} - T_{c}} \tag{14}$$

where $\overline{T_{s\text{-}aw}}$ and $\overline{T_{w\text{-}aw}}$ mean spanwise-averaged wall temperature and wall-averaged temperature. Dimensionless film cooling effectiveness (η_{ratio}) and dimensionless average cooling effectiveness ($\overline{\eta}_{ratio}$) are defined as:

$$\eta_{ratio} = \frac{\overline{\eta}}{\overline{\eta_0}} \tag{15}$$

$$\overline{\eta_{ratio}} = \frac{\frac{1}{n}\sum_{i=0}^{i=n}\overline{\eta}}{\frac{1}{n}\sum_{i=0}^{i=n}\overline{\eta_0}} \tag{16}$$

where $\overline{\eta_0}$ is the average film cooling effectiveness, and i is the point along the streamwise direction. The growth rate of wall-averaged cooling effectiveness is given as:

$$\Delta = \frac{\overline{\eta_w} - \overline{\eta_0}}{\overline{\eta_0}} \times 100\% \tag{17}$$

The dimensionless temperature is calculated by:

$$\Theta = \frac{T_{aw}}{T_\infty} \tag{18}$$

The streamwise velocity gradient and the normal velocity gradient are expressed as:

$$U^* = \frac{U}{U_\infty} \tag{19}$$

$$W^* = \frac{W}{U_\infty} \tag{20}$$

where U and W are streamwise velocity and normal velocity of airflow, respectively. To display vortices in a flow field, the equation for the Q criterion is given as [26]:

$$Q = -\frac{1}{2}[(\frac{\partial u}{\partial x})^2 + (\frac{\partial v}{\partial y})^2 + (\frac{\partial w}{\partial z})^2] - \frac{\partial u}{\partial y}\frac{\partial v}{\partial x} - \frac{\partial u}{\partial z}\frac{\partial w}{\partial x} - \frac{\partial v}{\partial z}\frac{\partial w}{\partial y} \tag{21}$$

where $\partial u_i/\partial x_j$ is a gradient of velocity in space. Streamwise gauge pressure and spanwise gauge pressure are calculated by:

$$P_f = P_{(f,i)} - P_0 \tag{22}$$

$$P_s = P_{(s,i)} - P_0 \tag{23}$$

where P_0 is atmospheric pressure, and P is actual pressure. f is a streamwise value, and s is a spanwise value.

2.4 Model validation

This section conducts an analysis of grid independence and validations of the turbulence model and the plasma model.

2.4.1 Grid independence analysis

Structural grids are used to set up the computational domain. The grids near the wall and film hole are refined to capture the complex flow phenomenon in the near-wall region. The y^+ value close to side walls is close to 1. With the plasma off, a minor difference in wall film cooling effectiveness is found among the cases with 0.5 million, 0.65 million, 1.30 million, and 2.60 million grids. Compared with the case with 1.30

million grids, the average deviations of cooling effectiveness for the cases with 0.65 million and 2.60 million grids are 1.4% and 0.2%, respectively, as shown in Fig. 4. Based on these facts, the number of 1.30 million grids is used for all simulations.

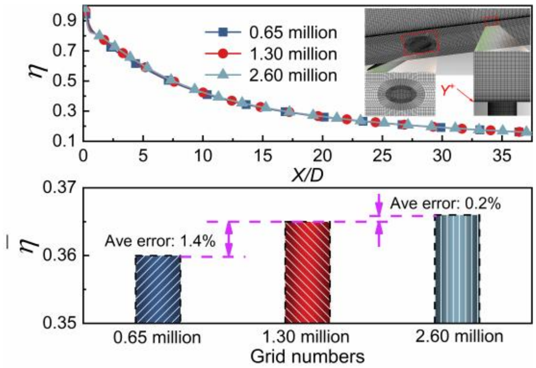

Fig. 4 Grid distributions near the film hole and analysis of grid independence

2.4.2 Validation of turbulence model

In a previous study [27], numerical results were conducted using the standard *k-ε* turbulence model, realizable *k-ε* turbulence model, and RNG *k-ε* turbulence model compared to experimental results by Sinha et al. [28]. The cooling effectiveness distributions on the wall centerlines for three turbulence models have the same trend as reported by Sinha et al. [28]. A minimum error of 2% is observed between the standard *k-ε* turbulence model and experimental results as shown in Fig. 5. The errors between other turbulence models and experimental results are above 10%. Accordingly, the standard *k-ε* turbulence model is used in the present simulations.

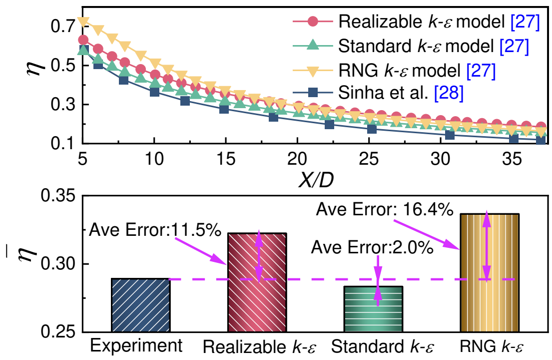

Fig. 5 Validation of turbulence models

2.4.3 Validation of plasma actuation model

The computational domain for the model validation has dimensions of 21.5 mm× 10 mm. The plasma actuators are under an applied voltage of 4 kV and an applied frequency of 3 kHz. Under the plasma actuation, the near-wall fluid downstream the actuator is speeded up. Deviations between simulation results and data in Shyy et al. [22] are 2.6% and 1.8% at inlet velocities of 5 m/s and 10 m/s, respectively, as shown in Fig. 6. These results indicate that the plasma actuation model in the present paper is reliable and acceptable.

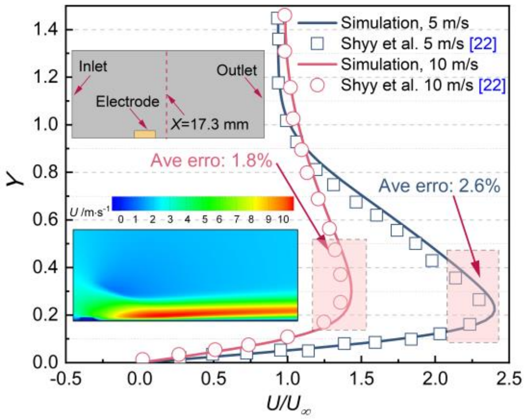

Fig. 6 Validations of plasma actuation model at various inlet velocities

3. Results and discussion

This section provides discussions about effects of comb plasma actuator (CPA) on tip and CPA on root on flow field, film cooling, and pressure loss.

3.1 Flow field characteristics

Fig. 7 presents dimensionless temperature distributions and streamlines at the streamwise planes 2*D* and 20*D* (in direction x). The low-temperature zone in the cross-section is concentrated in the spanwise range from -0.75 to 0.75. This zone decreases downstream the wall, and the temperature value increases under plasma off. Counter-rotating vortex pairs (CRVPs) emerge, and the coolant air is carried away from the wall and mixed with the high-temperature mainstream. This is the reason why the film cooling performance is significantly weakened. The core height of CRVPs increases along the streamwise direction, which enhances the enrolling effect of the mainstream on the coolant air. When the CPA is applied to the tip, the low-temperature zone is distributed in the whole spanwise direction. The low-temperature zone downstream the wall is enlarged compared to that under plasma off. The CPA on the tip produces anti-counter rotating vortex pairs (Anti-CRVPs), with a scale much larger than that of CRVPs. Anti-CRVPs weaken the strength of CRVPs, and the coolant air over the wall center diffuses to both sides. The distribution of spanwise film cooling is changed. Compared with plasma off, the temperature in the central region is lower in the case with the CPA on the tip. For the CPA on the root, the low-temperature zone downstream the wall is smaller than for the other two cases. It is observed that the core height of CRVPs for the CPA on the root is higher than that without plasma actuation. This indicates that the shape of the plasma actuator has a significant effect on the flow field distribution.

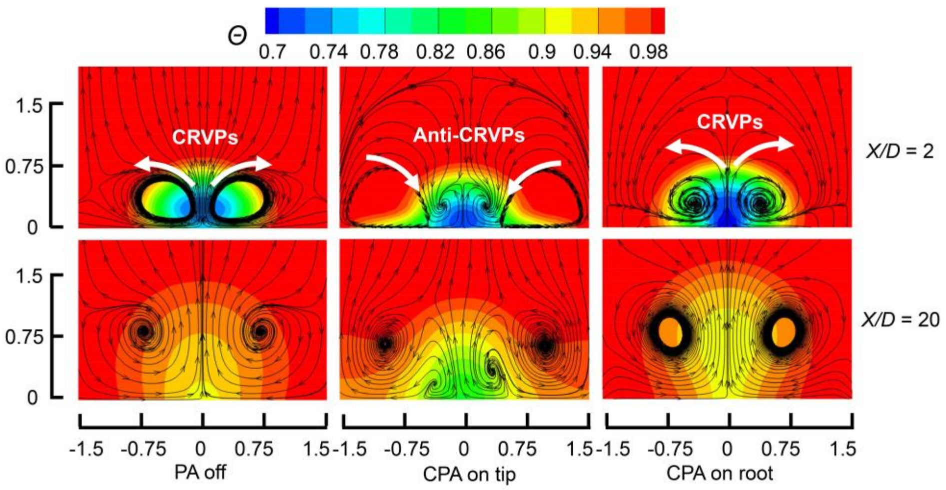

Fig. 7 Dimensionless temperature contours and streamlines at planes of $X = 2D$ and $20D$

Fig. 8 shows dimensionless streamwise velocity distributions and dimensionless normal velocities at the streamwise planes $2D$ and $20D$ (in direction x). Compared with the results under plasma actuation, the velocity boundary layer and the streamwise velocity become thicker and smaller under the plasma off. The streamwise fluid velocity near the wall increases under plasma actuation. The maximum velocity for the CPA on the tip is 1.2 times the mainstream velocity, which indicates that the near-wall fluid flow accelerates due to the presence of the plasma actuator. The flow velocity for the CPA on the root has a slight difference from that without plasma actuation. In contrast, the flow velocity for the CPA on the tip is significantly higher than that without plasma actuation. It is concluded that the CPA on the root shows a weak aerodynamic actuation effect on the flow field. The velocity boundary layer for the CPA on the tip is significantly thinner than for plasma off. The coolant air is pulled down to the wall due to the CPA on the tip. The maximum normal velocity for the CPA on the root has the largest height, which means the coolant air under the action of the CPA on the root shows a solid penetration to the mainstream.

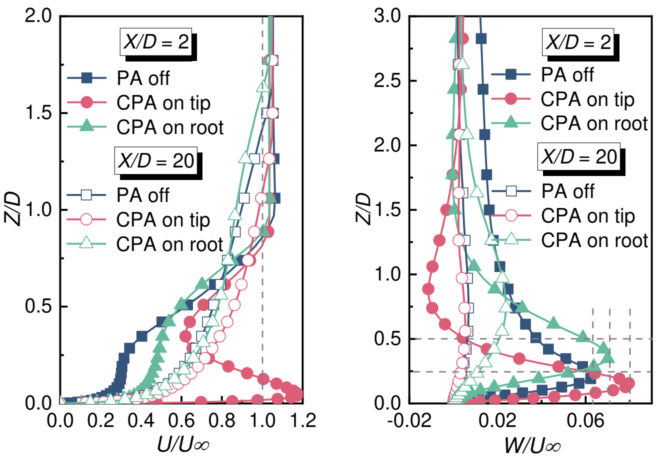

Fig. 8 Dimensionless velocity distributions at streamwise planes of $X = 2D$ and $20D$

3.2 Film cooling effectiveness

Fig. 9 presents the film cooling effectiveness distributions under different applied voltages at two low blowing ratios of 0.25 and 0.50. Compared with plasma off, film cooling effectiveness with the CPA on the tip has higher lateral distributions along the streamwise and spanwise directions. The body force for the CPA on the tip spreads the coolant air across the flat plate. The film cooling effectiveness of the CPA on the root is concentrated along the centerline close to the film hole. The body force from the CPA on the root extends the coolant air from the wall. For the CPA on the tip at the blowing ratio of 0.25, the widest film cooling effectiveness distribution is observed under an applied voltage of 12 kV. The film cooling effectiveness increases with the increase of applied voltage. A small difference under a blowing ratio of 0.50 is observed between the cooling effectiveness distributions at applied voltages of 12 kV and 24 kV. These results indicate that the CPA on the tip provides the best film cooling performance under an applied voltage of 12 kV at the low blowing ratios of 0.25 and 0.50. For the CPA on the root, the film cooling effectiveness distribution decreases along the streamwise direction with increasing applied voltage. High cooling effectiveness is mainly concentrated near the hole outlet, indicating that the CPA on the root improves the local film cooling performance close to the film hole at low blowing ratios.

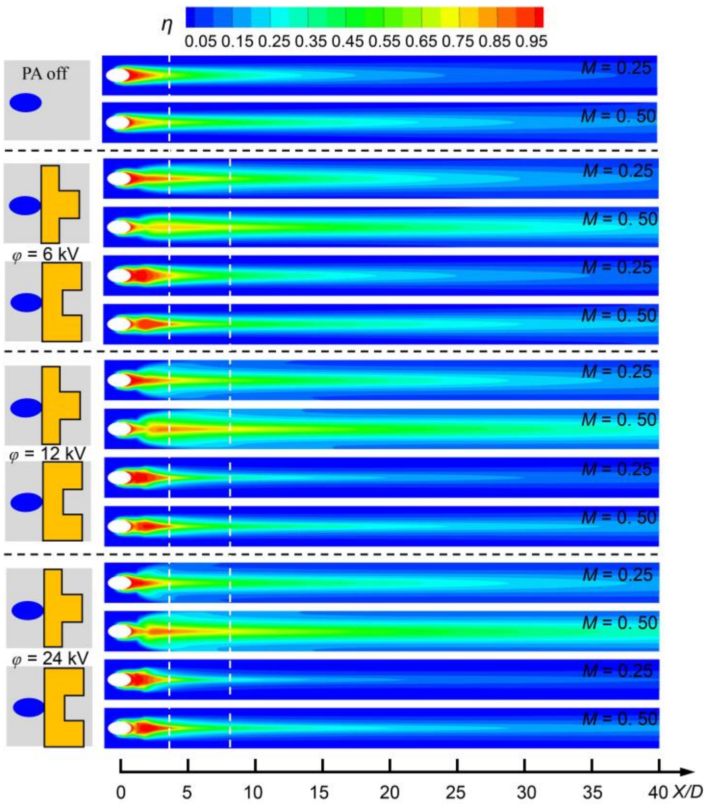

Fig. 9 Film cooling effectiveness distributions downstream the wall at low blowing ratios and applied voltages of 0, 6 kV, 12 kV, and 24 kV

Film cooling effectiveness distributions under different applied voltages are presented at high blowing ratios of 0.75 and 1.0 in Fig. 10. With the increase of the applied voltage, the cooling effectiveness distribution for the CPA on the tip increases along the streamwise and spanwise directions. The film cooling effectiveness is improved and covers the whole wall under the blowing ratios of 0.75 and applied voltage of 24 kV. A small area with less film cooling distributions appears near the hole outlet for the CPA on the tip at blowing ratios of 0.75 and 1.0. The coolant air has a considerable outlet momentum under high blowing ratios. The body force induced by the plasma actuator effectively weakens the suction effect of the mainstream on the coolant air under a high voltage of 24 kV. This indicates that the plasma actuator has a wall-jet impact on the airflow. The cooling effectiveness distribution near the film hole (until 7.5D) for the CPA on the root is improved compared to that without plasma actuation. The film cooling downstream the wall deteriorates under high blowing ratios. The results clearly indicate that the CPA on the root is not suitable for improving the overall film cooling performance.

Comparisons of spanwise-averaged film cooling effectiveness are conducted under different applied voltages and are provided in Fig. 11. The spanwise-averaged cooling effectiveness for the CPA on the tip is higher than that with plasma off at low blowing ratios (such as 0.25 and 0.5). The CPA on the tip under applied voltages of 6 kV, 12 kV, and 24 kV shows 1.53-1.67 times, 1.88-1.94 times, and 1.77-2.01 times film cooling effectiveness for plasma off. The flat plate obtains the best overall film cooling performance for the CPA on the tip at an applied voltage of 12 kV, but minor enhancement of cooling effectiveness is observed under the high applied voltage of 24 kV. The CPA on the root is 1.16-1.27 times the cooling effectiveness for plasma off at the applied voltage of 6 kV and low blowing ratios (0.25 and 0.5). Accordingly, it is proved that the CPA on the root increases the film cooling performance under low blowing ratio and low applied voltage. The CPA on the tip at the high blowing ratios of 0.75 and 1.0 shows 0.95-1.20 times, 1.36-1.78 times, and 2.01-2.16 times the film cooling effectiveness for the plasma off under applied voltages of 6 kV, 12 kV, and 24 kV. The increase in applied voltage enhances the aerodynamic actuation effect. Strong aerodynamic induction effectively weakens the considerable outlet momentum of the coolant air and the entrainment of high-temperature mainstream to the coolant air. The film cooling downstream the wall deteriorates for the CPA on the root at high blowing ratios. The film cooling effectiveness is significantly improved by placing the CPA on the tip, while the CPA on the root has a poor effect on cooling performance under low blowing ratios. The reduction of overall momentum enhances the mixing degree between mainstream and coolant air.

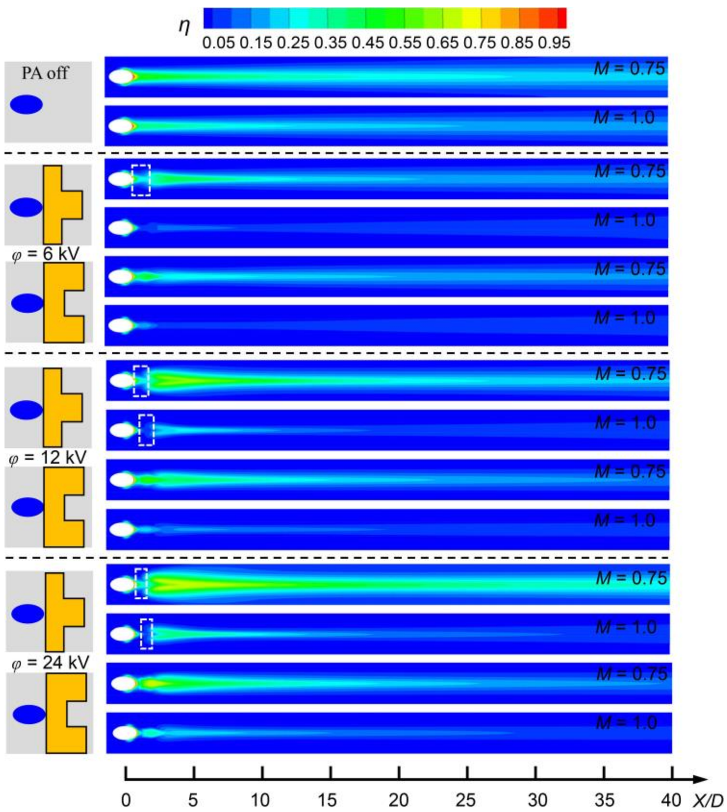

Fig. 10 Film cooling effectiveness distributions downstream the wall at high blowing ratios and applied voltages of 0, 6 kV, 12 kV and 24 kV

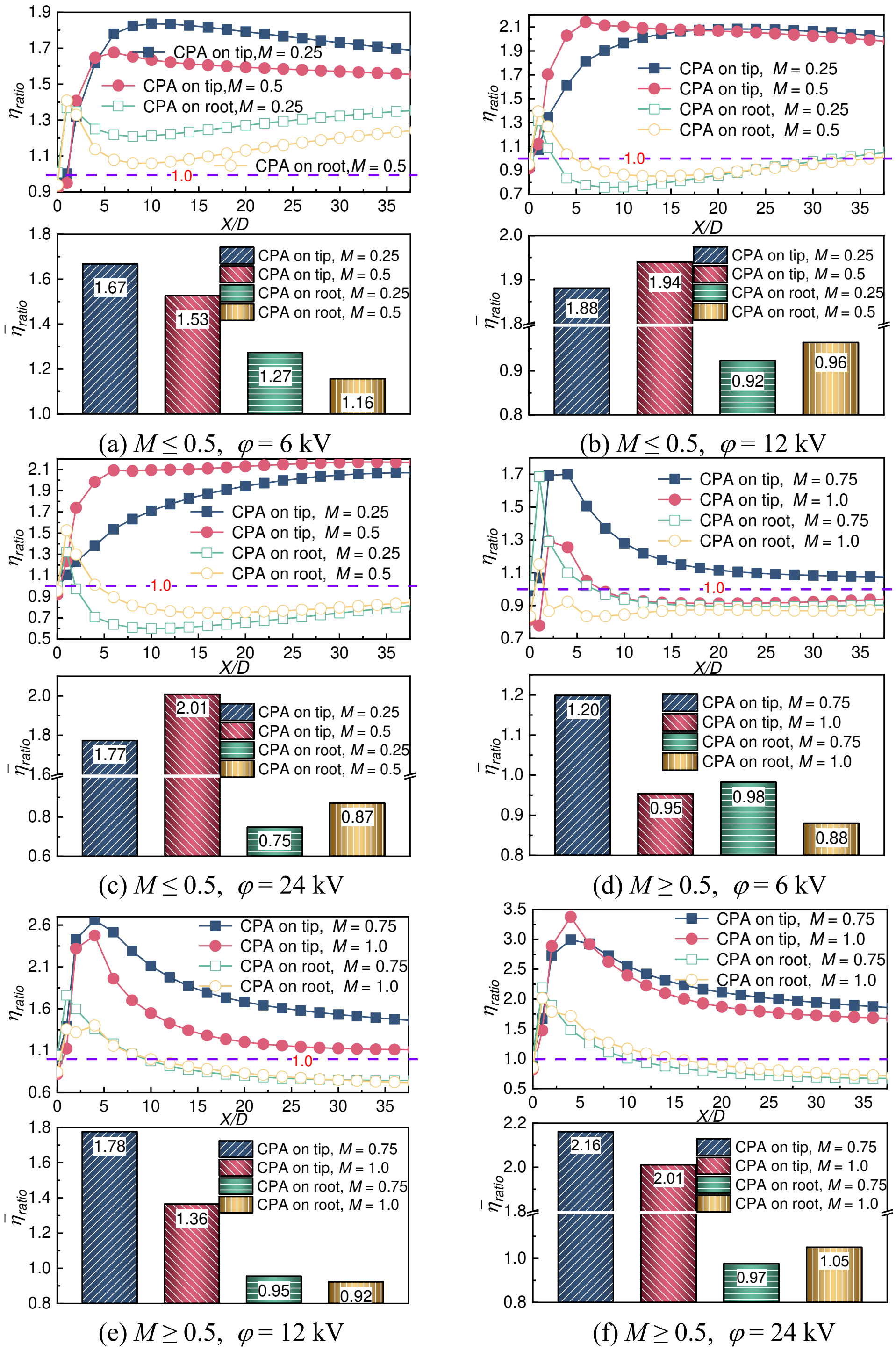

Fig. 11 Comparisons of spanwise-averaged film cooling effectiveness at different applied voltages

Fig. 12 shows spanwise film cooling effectiveness under different blowing ratios. The body force for the CPA on the tip diffuses along the spanwise direction. Table 3 provides growth rates of average spanwise film cooling effectiveness for the CPA on the tip. The average spanwise cooling effectiveness of CPA on the tip increases by

103.4%, 164.6%, and 150.5% at blowing ratios of 0.5, 0.75, and 1.0. The spanwise film cooling effectiveness for the CPA on the root is higher than without plasma only at high blowing ratios. The film cooling deteriorates under low blowing ratios, related to the body force along the center for the CPA on the root. These results prove that the shape of the plasma actuator significantly affects the spanwise film cooling, which provides an approach for increasing the inlet temperature of the gas turbine.

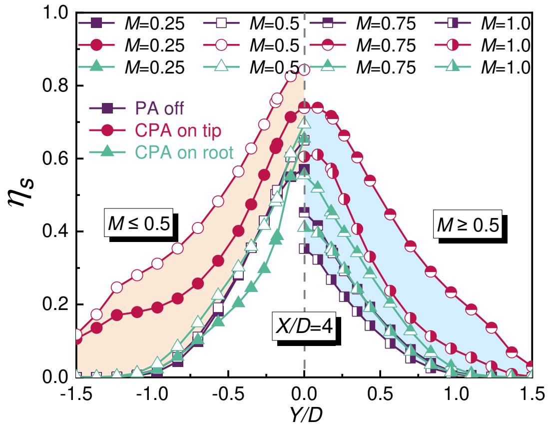

Fig. 12 Comparisons of spanwise film cooling effectiveness at different blowing ratios and applied voltage of 12 kV

Table 3. Growth rates of average spanwise cooling effectiveness

Case	$M = 0.25$	$M = 0.5$	$M = 0.75$	$M = 1.0$
$\overline{\eta}_s$ of PA off	0.223	0.234	0.161	0.111
$\overline{\eta}_s$ of CPA on tip	0.362	0.476	0.426	0.278
$\overline{\eta}_s$ of growth rate of CPA on tip	62.3%	103.4%	164.6%	150.5%
$\overline{\eta}_s$ of CPA on root	0.188	0.243	0.218	0.157
$\overline{\eta}_s$ of growth rate of CPA on root	-15.75	3.8%	35.4%	41.4%

Fig. 13 shows wall-averaged film cooling effectiveness under different factors. The arrangement of the CPA on the tip achieves the optimal performance of the overall film cooling. Compared with plasma off under blowing ratios of 0.25 and 1.0, the wall-averaged cooling effectiveness for the CPA on the tip increases by 38.0% and 108.8%.

Compared with plasma off, the cooling performance for the CPA on the root deteriorates under all blowing ratios. For various working conditions, the film cooling effectiveness reaches the highest values under the blowing ratio of 0.5. The wall-averaged cooling effectiveness of the CPA on the tip increases by 58.7%, 108.8%, and 115.0% compared to that without plasma actuation under applied voltages of 6 kV, 12 kV, and 24 kV. The wall-averaged cooling effectiveness at the applied voltage of 12 kV is 31.6% higher than that at 6 kV, whereas the value at 24 kV is only 2.9% higher than that at 12 kV. These results indicate that the applied voltage has the optimal value for improving film cooling effectiveness. With a small amount of coolant air, the best film cooling performance of the flat wall is reached under the blowing ratio of 0.5 and the applied voltage of 12 kV.

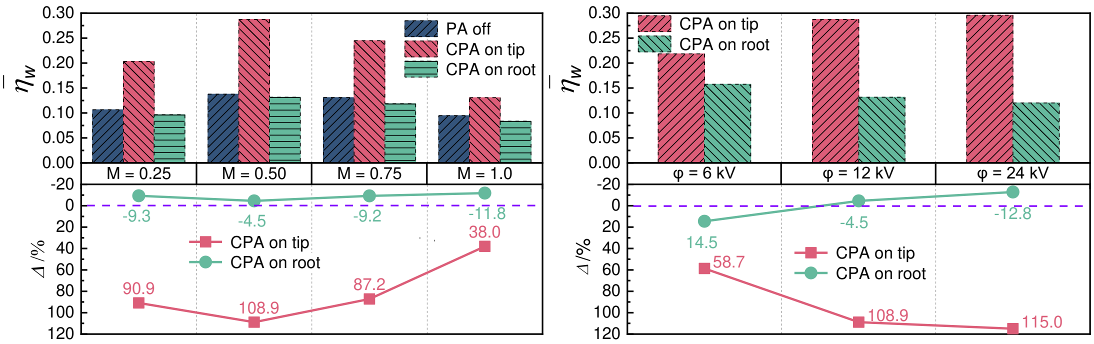

(a) Various blowing ratio (b) Various applied voltage

Fig. 13 Comparisons of wall-averaged film cooling effectiveness under different factors

3.3 Pressure loss

Three-dimensional vortex structures are displayed with dimensionless temperature contours as shown in Fig. 14. Counter rotating vortex pairs (CRVPs) at low temperature are presented near the hole outlet, reflecting the mixing degree of the mainstream and the coolant air. Anti-counter rotating vortex pairs (anti-CRVPs) at high temperature are presented on both sides downstream the hole, reflecting the disturbance effect on the mainstream. The dimension of anti-CRVPs for the CPA on the tip is larger than for CRVPs. The presence of the anti-CRVPs improves the diffusion of the coolant air from the hole outlet to both sides, which weakens the intensity of the CRVPs. Compared with plasma off, the dimension of CRVPs on the wall centerline for the CPA on the tip is reduced due to plasma actuation. The vortex dimension of the CPA on the root is larger than with plasma off, intensifying the mixing of the mainstream at high temperature and the coolant air at low temperature.

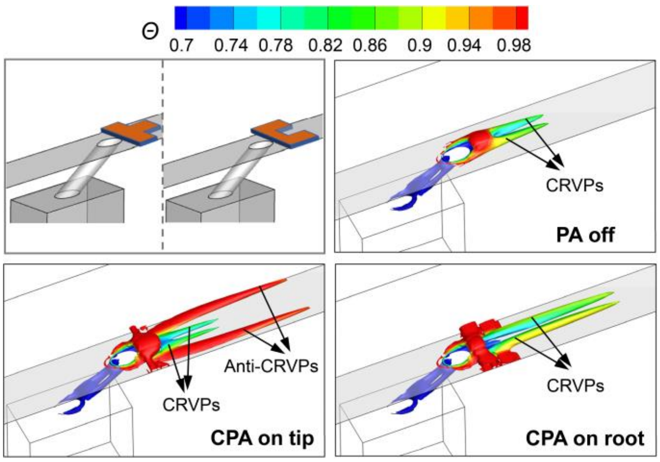

Fig. 14 Three-dimensional vortex structures at blowing ratio of 0.5 and applied voltage of 12 kV based on the Q criterion

Fig. 15 presents pressure distributions (gauge pressure) under a blowing ratio of 0.5 and an applied voltage of 12 kV. Streamwise pressure on the wall surface increases dramatically under plasma actuation. The pressure for the CPA on the tip increases by 0.18% compared to that with plasma off. The airflow is forced down to the wall by the plasma aerodynamic actuation. The streamwise pressure variation for the CPA on the root is smaller than that for the CPA on the tip, which indicates that the CPA on the root has less disturbance on the streamwise airflow. The spanwise pressure on the wall center sharply decreases due to the presence of the comb plasma actuator, and the flow velocity increases according to the Bernoulli equation. The CPA on the tip has five inflection points between -1.5 D and 1.5 D along the Y direction, and the pressure value is lower than that of the CPA on the root.

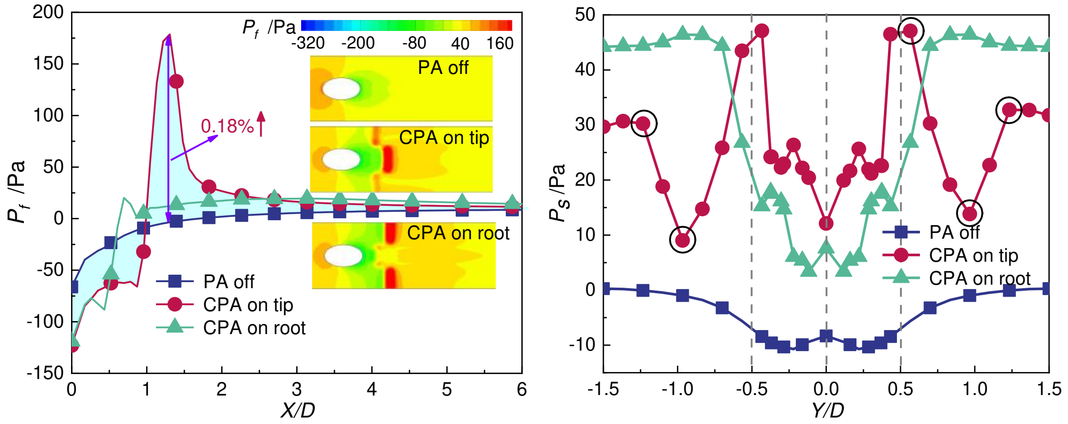

(a) Streamwise gauge pressure (b) Spanwise gauge pressure

Fig. 15 Gauge pressure distributions at blowing ratio of 0.5 and applied voltage of 12 kV

4 Conclusions

Effects of applied voltage and actuator shape on the flow field and film cooling effectiveness were investigated under blowing ratios of 0.25, 0.5, 0.75, and 1.0. The main conclusions are summarized as follows:

(1) For the comb plasma actuator (CPA) on the tip, the spanwise expansion of the body force causes anti-counter rotating vortex pairs (anti-CRVPs) with a larger scale than CRVPs. The anti-CRVPs significantly weaken the lifting effect of the mainstream on the coolant air. The aerodynamic actuation of plasma accelerates the near-wall fluid flow effectively. The dimension and core height of CRVPs increase due to the agminated body force for the CPA on the root. The coolant air causes the arched distribution, which deteriorates the film cooling.

(2) The CPA on the tip significantly improves the film cooling effectiveness. For the CPA on the tip under applied voltages of 12 kV, the wall-averaged values of cooling effectiveness are 90.9, 108.8%, 87.2%, and 38.0% higher than those without plasma

at blowing ratios of 0.25, 0.5, 0.75, and 1.0. Compared with plasma off, the wall-averaged values of cooling effectiveness increase by 58.7%, 108.8%, and 115.0% under applied voltages of 6 kV, 12 kV, and 24 kV. Spanwise film cooling effectiveness of CPA on tip increases from 62.3% to 164.6% under blowing ratios from 0.5 to 1.0.

(3) The film cooling effectiveness of the CPA on the root increases by 14.5% under 6 kV applied voltage and 0.25 blowing ratio compared with plasma off. The film cooling performance is improved near the hole outlet for the CPA on the root. The wall temperature is significantly reduced by optimizing the shape of the plasma actuator.

5 Acknowledgments

This work is supported by the Natural Science Foundation of Hebei Province of China (Grant No. E2021202163), the Science Fund for Distinguished Young Scholars of Hebei Province (Grant No. E2022202139), the Special Project of Science and Technology Winter Olympics in the Hebei Technology Innovation Guidance Plan (Grant No. 21474501D), and the Foundation of Key Laboratory of Thermo-Fluid Science and Engineering (Xi’an Jiaotong University), Ministry of Education, Xi’an 710049, P.R. China (Grant No. KLTFSE2018KFJJ01).

References

[1] Kumar R, Ismail M, Zhao W, Noori M, Yadav AR, Chen SB, Singh V, Altabey WA, Silik AIH, Kumar G, Kumar J, Balodi A (2021) Damage detection of wind turbine system based on signal processing approach: a critical review. Clean Technol. Environ. Policy 23: 561-580.

[2] Wang WJ, Tang Q, Gao B (2022) Exploration of CO_2 emission reduction pathways: identification of influencing factors of CO_2 emission and CO_2 emission reduction potential of power industry. Clean Technol. Environ. Policy. https://doi.org/10.1007/s10098-022-02456-1

[3] Pirkandi J, Khodaparast S, Ommian M, Abbasi Y (2020) Analyzing the thermodynamic performance of a hybrid system consisting of a gas turbine and two Stirling engines in series and parallel configurations. Clean Technol. Environ. Policy 22: 1385-1403.

[4] Sun J, Zhang FX, Wang J, Baleta J, Xie GN, Sundén B (2022) Effect of dielectric barrier discharge plasma on film cooling performance. Therm. Sci. 26 (5B): 4157-4168.

[5] He J, Deng Q, Feng Z (2021) Film cooling performance enhancement by upstream V-shaped protrusion/dimple vortex generator. Int. J. Heat Mass Transfer 180: 121784.

[6] Huang X, Pu J, Zhang T, Wang JH, Wu WL, Wu XY (2022) Effect of length-to-diameter ratio on film cooling and heat transfer performances of simple and compound cylindrical-holes in transverse trenches with various depths. Int. J. Heat Mass Transfer 185: 122328.

[7] Abdollahzadeh M, Páscoa JC, Oliveira PJ (2014) Modified split-potential model for modeling the effect of DBD plasma actuators in high altitude flow control. Curr. Appl. Phys. 14: 1160-1170.

[8] Rodrigues FF, Mushyam A, Pascoa JC, Trancossi M (2019) A new plasma actuator configuration for improved efficiency: the stair-shaped dielectric barrier discharge actuator. J. Phys. D: Appl. Phys. 52: 120317.

[9] Rodrigues FF, Pascoa JC, Trancossi M (2016) Analysis of innovative plasma actuator geometries for boundary layer control. In: Proceedings of the ASME 2016 international mechanical engineering congress and exposition, IMECE2016-66495.

[10] Li GZ, Zhang HJ, Yan WW (2019) Control of the coherent structure dynamics of a film cooling flow by plasma aerodynamic actuation. Int. J. Heat Mass Transfer 137: 434-445.

[11] Zhang X, Cui YD, Tay CMJ, Khoo BC (2021) Flow field generated by a dielectric barrier discharge plasma actuator in quiescent air at initiation stage. Chin. J. Aeronaut. 34: 13-24.

[12] Chen JL, Liao YH (2021) Effects of an annular plasma actuator on a co-flow jet downstream of a bluff-body. Appl. Therm. Eng 192: 116975.

[13] Harinaldi, Kesuma MD, Irwansyah R, Julian J, Satyadharma A (2020) Flow control with multi-DBD plasma actuator on a delta wing. Evergreen: Jt. J. Novel Carbon Resour. Sci. Green Asia Strategy 7: 602-608.

[14] Huang G, Dai Y, Yang C, Wu Y, Xia Y (2021) Effect of dielectric barrier discharge plasma actuator on the dynamic moment behavior of pitching airfoil at low Reynolds number. Phys. Fluids. 33: 043603.

[15] Zheng JG, Cui YD, Khoo BC (2019) A comparative study of alternating current and nanosecond plasma actuators in flow separation control. Int. J. Heat Mass Transfer 135: 1097-1117.

[16] Giorgi MGD, Pescini E, Marra F, Ficarella A (2016) Plasma actuator scaling down to improve its energy conversion efficiency for active flow control in modern turbojet engines compressors. Appl. Therm. Eng 106: 334-350.

[17] Sun J, Xie GN, Wang J, Sundén B (2022) Enhanced film cooling and flow disturbance of an AGTB turbine cascade with plasma aerodynamic actuation at film-holes outlets. Int. Commun. Heat Mass Transfer. https://doi.org/10.1016/j.icheatmasstransfer.2022.106522

[18] Dai SJ (2015) An experimental study of plasma aerodynamic actuation on a round jet in cross flow. AIP Adv. 5: 037143.

[19] Erfani R, Zare-Behtash H, Kontis K (2012) Plasma actuator: Influence of dielectric surface temperature. Exp. Therm. Fluid Sci. 42: 258-264.

[20] Li GZ, Huang YJ, Zhang HJ, Yan WW, Nie DM (2021) Numerical comparison of saw-tooth plasma actuators for film cooling flow control over a flat plate. Int. J. Therm. Sci. 163: 106807.

[21] Durscher RJ, Roy S (2012) Three-dimensional flow measurements induced from serpentine plasma actuators in quiescent air. J. Phys. D: Appl. Phys. 45: 035202.

[22] Shyy W, Jayaraman B, Andersson A (2002) Modeling of glow discharge-induced fluid dynamics. J. Appl. Phys. 92: 6434-6443.

[23] Sun J, Zhang FX, Wang J, Xie GN, Sundé B (2022) Effects of plasma actuation and hole configuration on film cooling performance. Propul. Power Res. https://doi.org/10.1016/j.jppr.2022.03.005..

[24] Versteeg HK, Malalasekera W (1995) An introduction to computational fluid dynamics: the finite volume method, first edition, Longman, London.

[25] Goldstein RJ, Eckert ERG, Bljrgcira F (1974) Effects of hole geometry and denstty on three-dimensional film cooling. Int. J. Heat Mass Transfer 17: 595-607.

[26] Silva CBD, Pereira JCF (2008) Invariants of the velocity-gradient, rate-of-strain, and rate-of-rotation tensors across the turbulent/nonturbulent interface in jets. Phys. Fluids. 20: 055101.

[27] Wang J, Liu C, Zhao ZM, Baleta J, Sundén B (2020) Effect and optimization of backward hole parameters on film cooling performance by Taguchi method. Energy Convers. Manage 214: 112809.

[28] Sinha AK, Bogard DG, Crawford ME (1991) Film-cooling effectiveness downstream of a single row of holes with variable density ratio. Trans. ASME: J. Turbomachin. 113: 442-449.

Captions of figures and tables

Fig. 1 Three-dimensional computational domain

Fig. 2 Arrangements and body force distributions of comb plasma actuators

Fig. 3 Schematic diagram of the plasma aerodynamic actuation

Fig. 4 Grid distributions near the film hole and analysis of grid independence

Fig. 5 Validation of turbulence models

Fig. 6 Validations of plasma actuation model at various inlet velocities

Fig. 7 Dimensionless temperature contours and streamlines at planes of X = 2D and 20D

Fig. 8 Dimensionless velocity distributions at streamwise planes of X = 2D and 20D

Fig. 9 Film cooling effectiveness distributions downstream the wall at low blowing ratios and applied voltages of 0, 6 kV, 12 kV, and 24 kV

Fig. 10 Film cooling effectiveness distributions downstream the wall at high blowing ratios and applied voltages of 0, 6 kV, 12 kV and 24 kV

Fig. 11 Comparisons of spanwise-averaged film cooling effectiveness at different applied voltages

Fig. 12 Comparisons of spanwise film cooling effectiveness at different blowing ratios and applied voltage of 12 kV

Fig. 13 Comparisons of wall-averaged film cooling effectiveness under different factors

Fig. 14 Three-dimensional vortex structures at blowing ratio of 0.5 and applied voltage of 12 kV based on the Q criterion

Fig. 15 Gauge pressure distributions at blowing ratio of 0.5 and applied voltage of 12 kV

Table 1 Parameters of comb plasma actuators

Table 2 Boundary conditions of simulations

Table 3 Growth rates of average spanwise cooling effectiveness